Extending the emission wavelength of Ge nanopillars to 2.25 μm using silicon nitride stressors

R.W. Millar,[1] K. Gallacher,[1] A. Samarelli,[1] J. Frigerio,[2] D. Chrastina,[2] G. Isella,[2] T. Dieing[3] and D.J. Paul[1*]

[1]*School of Engineering, University of Glasgow, Rankine Building, Oakfield Avenue, Glasgow, G12 8LT, UK*

[2]*L-NESS, Politecnico di Milano, Via Anzani 42, 22100, Como, Italy*

[3]*WiTec GmbH, Lise-Meitner-Str. 6, 89081 Ulm, Germany*

[*]*Douglas.Paul@glasgow.ac.uk*

Abstract: The room temperature photoluminescence from Ge nanopillars has been extended from 1.6 μm to above 2.25 μm wavelength through the application of tensile stress from silicon nitride stressors deposited by inductively-coupled-plasma plasma-enhanced chemical-vapour-deposition. Photoluminescence measurements demonstrate biaxial equivalent tensile strains of up to $\sim$ 1.35% in square topped nanopillars with side lengths of 200 nm. Biaxial equivalent strains of 0.9% are observed in 300 nm square top pillars, confirmed by confocal Raman spectroscopy. Finite element modelling demonstrates that an all-around stressor layer is preferable to a top only stressor, as it increases the hydrostatic component of the strain, leading to an increased shift in the band-edge and improved uniformity over top-surface only stressors layers.

OCIS codes: (130.3130) Integrated optics materials; (130.5990) Semiconductors; (130.3120) Integrated optics devices; (220.4241) Nanostructure fabrication; (250.5230) Photoluminescence.

References and links

1. G. T. Reed, ed., *Silicon Photonics: The State of the Art* (John Wiley & Sons Ltd., 2008).
2. D. J. Paul, "Silicon photonics: a bright future?," Electron. Lett. **45,** 582–584 (2009).
3. J. Liu, X. Sun, R. Camacho-Aguilera, L. C. Kimerling, and J. Michel, "Ge-on-Si laser operating at room temperature," Opt. Lett. **35**, 679–81 (2010).
4. R. E. Camacho-Aguilera, Y. Cai, N. Patel, J. T. Bessette, M. Romagnoli, L. C. Kimerling, and J. Michel, "An electrically pumped germanium laser," Opt. Express **20**, 11316–11320 (2012).
5. K. Gallacher, P. Velha, D. J. Paul, S. Cecchi, J. Frigerio, D. Chrastina, and G. Isella, "1.55 μm direct bandgap electroluminescence from strained n-Ge quantum wells grown on Si substrates," Appl. Phys. Lett. **101**, 211101–211101–4 (2012).
6. P. Chaisakul, D. Marris-Morini, J. Frigerio, D. Chrastina, M.-S. Rouifed, S. Cecchi, P. Crozat, G. Isella, and L. Vivien, "Integrated germanium optical interconnects on silicon substrates," Nature Photon. **8**, 482–488 (2014).
7. J. Michel, J. Liu, and L. C. Kimerling, "High-performance Ge-on-Si photodetectors," Nature Photon. **4**, 527–534 (2010).
8. R. Warburton, G. Intermite, M. Myronov, P. Allred, D. Leadley, K. Gallacher, D. Paul, N. Pilgrim, L. Lever, Z. Ikonic, R. Kelsall, E. Huante-Ceron, A. Knights, and G. Buller, "Ge-on-Si single-photon avalanche diode detectors: Design, modeling, fabrication, and characterization at wavelengths 1310 and 1550 nm," IEEE Trans. Electron Devices **60**, 3807–3813 (2013).
9. Y. H. Kuo, Y. K. Lee, Y. S. Ge, S. Ren, J. E. Roth, T. I. Kamins, D. A. B. Miller, and J. S. Harris, "Strong quantum-confined Stark effect in germanium quantum-well structures on silicon," Nature **437**, 1334–1336 (2005).

#235529 Received 12 Mar 2015; revised 14 Apr 2015; accepted 3 May 2015; published 6 Jul 2015

10. D. C. S. Dumas, K. Gallacher, S. Rhead, M. Myronov, D. R. Leadley, and D. J. Paul, "Ge/SiGe quantum confined Stark effect electro-absorption modulation with low voltage swing at $\lambda = 1550$ nm," Opt. Express **22**, 19284–19292 (2014).
11. J. R. Sanchez-Perez, C. Boztug, F. Chen, F. F. Sudradjat, D. M. Paskiewicz, R. Jacobson, M. G. Lagally, and R. Paiella, "Direct-bandgap light-emitting germanium in tensilely strained nanomembranes," Proc. Natl. Acad. Sci. U.S.A. **108**, 18893–18898 (2011).
12. J. R. Jain, A. Hryciw, T. M. Baer, M. L. Brongersma, and R. T. Howe, "A micromachining-based technology for enhancing germanium light emission via tensile strain," Nature Photon. **6**, 398–405 (2012).
13. M. J. Suess, R. Geiger, R. A. Minamisawa, G. Schiefler, J. Frigerio, D. Chrastina, G. Isella, R. Spolenak, J. Faist, and H. Sigg, "Analysis of enhanced light emission from highly strained germanium microbridges," Nature Photon. **7**, 466–472 (2013).
14. A. Ghrib, M. El Kurdi, M. de Kersauson, M. Prost, S. Sauvage, X. Checoury, G. Beaudoin, I. Sagnes, and P. Boucaud, "Tensile-strained germanium microdisks," Appl. Phys. Lett. **102**, 221112 (2013).
15. A. Ghrib, M. El Kurdi, M. Prost, S. Sauvage, X. Checoury, G. Beaudoin, M. Chaigneau, R. Ossikovski, I. Sagnes, and P. Boucaud, "All-around SiN stressor for high and homogeneous tensile strain in germanium microdisk cavities," Adv. Opt. Mater. **3**, 353–358 (2015).
16. A. Ghrib, M. de Kersauson, M. El Kurdi, R. Jakomin, G. Beaudoin, S. Sauvage, G. Fishman, G. Ndong, M. Chaigneau, R. Ossikovski, I. Sagnes, and P. Boucaud, "Control of tensile strain in germanium waveguides through silicon nitride layers," Appl. Phys. Lett. **100**, 201104 (2012).
17. G. Capellini, C. Reich, S. Guha, Y. Yamamoto, M. Lisker, M. Virgilio, A. Ghrib, M. E. Kurdi, P. Boucaud, B. Tillack, and T. Schroeder, "Tensile Ge microstructures for lasing fabricated by means of a silicon complementary metal-oxide-semiconductor process," Opt. Express **22**, 399–410 (2014).
18. M. V. Fischetti and S. E. Laux, "Band structure, deformation potentials, and carrier mobility in strained Si, Ge, and SiGe alloys," J. Appl. Phys. **80**, 2234–2252 (1996).
19. D. J. Paul, "Si/SiGe heterostructures: from material and physics to devices and circuits," Semicond. Sci. Technol. **19**, R75 (2004).
20. G. Isella, D. Chrastina, B. Rössner, T. Hackbarth, H.-J. Herzog, U. König, and H. von Känel, "Low-energy plasma-enhanced chemical vapor deposition for strained Si and Ge heterostructures and devices," Solid-State Electron. **48**, 1317–1323 (2004).
21. R. Geiger, J. Frigerio, M. J. Süess, D. Chrastina, G. Isella, R. Spolenak, J. Faist, and H. Sigg, "Excess carrier lifetimes in Ge layers on Si," Appl. Phys. Lett. **104**, 062106 (2014).
22. R. Camacho-Aguilera, Z. Han, Y. Cai, L. C. Kimerling, and J. Michel, "Direct band gap narrowing in highly doped Ge," Appl. Phys. Lett. **102**, 152106 (2013).
23. M. M. Mirza, H. Zhou, P. Velha, X. Li, K. E. Docherty, A. Samarelli, G. Ternent, and D. J. Paul, "Nanofabrication of high aspect ratio ($\sim$50:1) sub-10 nm silicon nanowires using inductively coupled plasma etching," J. Vac. Sci. Technol., B **30**, 06FF02 (2012).
24. F. Pezzoli, F. Isa, G. Isella, V. Falub, C. T. Kreiliger, M. Salvalaglio, R. Bergamaschini, E. Grilli, M. Guzzi, H. von Känel, and L. Miglio, "Ge crystals on si show their light," Phys. Rev. Appl. **1**, 044005 (2014).
25. D. J. Paul, "8-band **k**.**p** modeling of the quantum confined Stark effect in Ge quantum wells on Si substrates," Phys. Rev. B **77**, 155323 (2008).
26. D. Nam, D. Sukhdeo, and S. Gupta, "Study of carrier statistics in uniaxially strained Ge for a low-threshold Ge laser," IEEE J. Sel. Topics Quantum Electron. **20**, 1500107 (2014).
27. S. A. Lynch, D. J. Paul, P. Townsend, G. Matmon, Z. Suet, R. W. Kelsall, Z. Ikonic, P. Harrison, J. Zhang, D. J. Norris, A. G. Cullis, C. R. Pidgeon, P. Murzyn, B. Murdin, M. Bain, H. S. Gamble, M. Zhao, and W.-X. Ni, "Toward silicon-based lasers for terahertz sources," IEEE J. Sel. Topics Quantum Electron. **12**, 1570–1578 (2006).
28. D. J. Paul, "The progress towards terahertz quantum cascade lasers on silicon substrates," Laser Photon. Rev. **4**, 610–632 (2010).
29. D. J. Lockwood and J. F. Young, *Light Scattering in Semiconductor Structures and Superlattices*, David J. Lockwood and Jeff F. Young, eds. (Springer, 1991).
30. C.-Y. Peng, C.-F. Huang, Y.-C. Fu, Y.-H. Yang, C.-Y. Lai, S.-T. Chang, and C. W. Liu, "Comprehensive study of the Raman shifts of strained silicon and germanium," J. Appl. Phys. **105**, 083537 (2009).
31. I. De Wolf, H. E. Maes, and S. K. Jones, "Stress measurements in silicon devices through Raman spectroscopy: Bridging the gap between theory and experiment," J. Appl. Phys. **79**, 7148–7156 (1996).

1. Introduction

Germanium has received significant attention as an optical material in recent years, as it has the potential to enable active, CMOS compatible, photonics components [1, 2]. It has a direct bandgap (Γ-valley) which is only 140 meV larger than the indirect bandgap, allowing for the potential of emitters such as lasers [3, 4] and LEDs [5], as well as waveguides [6], photodetec-

#235529 Received 12 Mar 2015; revised 14 Apr 2015; accepted 3 May 2015; published 6 Jul 2015

tors [7, 8], and modulators [9, 10], all on a Si platform. With high degenerate n-type doping the Fermi level can be moved near to the Γ-valley, resulting in either optically or electrically injected carriers having a higher probability of recombining radiatively at this band; both electrically and optically pumped Ge lasers have been demonstrated by this technique [3, 4]. The application of biaxial tensile strain in the (100) plane has been predicted, and demonstrated, to move the Γ-valley to lower energies at a greater rate than the L-valley, therefore increasing the carrier concentration at the Γ-valley, and lowering the n-type doping required for optical gain [11]. This in turn reduces the free carrier absorption and should lead to a Ge laser with a lower threshold and higher slope efficiency. Furthermore, the direct band absorption wavelength of strained Ge photodiodes can be red-shifted, either for photodetection at energies below the unstrained band-edge, or in order to have increased direct bandgap absorption at 1.55 μm, allowing for more compact devices.

Optical emission from strained Ge has been demonstrated in a number of ways, for example, with mechanically strained membranes [11], micro-machined structures [12], micro bridge structures [13], and silicon nitride stressor layers applied to Ge microdisks [14, 15] and Ge waveguides [16, 17]. The use of silicon nitride as a stressor layer is especially interesting, as it is already used in CMOS processes for strained Si channels, and therefore it is of interest to investigate the limits of this approach.

This paper demonstrates photoluminescence up to 2.25 μm from 200 nm square top Ge pillars with biaxial equivalent tensile strain of ∼1.35% applied using silicon nitride stressors. Furthermore, finite element modelling demonstrates that for this pillar geometry, an all around stressor layer is preferable to a top-surface only stressor. The presence of silicon nitride on the sidewalls prevents the compression in the *z*-direction that is usually caused from tensile strain in the top plane, therefore increasing the hydrostatic component of the strain tensor. This has the effect of lowering the energy of the Γ-valley conduction band at a greater rate [18, 19] than pillars with only a pure biaxial strain from a top-surface stressor.

2. Growth and material properties

A low-energy plasma-enhanced chemical vapour deposition (LEPECVD) tool was used to grow 500 nm of n-type Ge on a 100 mm p-Si (100) wafer [20]. Hall-bar measurements at 300 K were used to confirm the active, in-situ, phosphorus degenerate doping density of $N_D \sim 2.5 \times 10^{19}$ cm^{-3}. No cycling annealing was performed on the material, in order to avoid dopant clustering and out-diffusion [21], which in conjunction with the low growth temperature of 500 °C, results in low levels of tensile strain from the thermal mismatch between Ge and Si. Raman spectroscopy measurements confirm that the strain in the Ge epilayer is negligible.

The degenerate n-type doping of $N_D \sim 2.5 \times 10^{19}$ cm^{-3} leads to a bandgap narrowing (BGN) of ∼32 meV corresponding to a redshift of ∼ 64 nm from 1.55 μm, as measured by photoluminescence. This is consistent with the findings of Camacho-Aguilera et al. in [22], when taking into account that their model includes a small amount of strain from growth, which is not present in the material used in this publication. Given the lack of data in the literature regarding BGN from doping at high strain levels, in this work it has been assumed to be a constant energy reduction over all strain levels measured.

3. Fabrication

Separate 1 × 1 mm sized arrays of 300 × 300 and 200 × 200 nm squares were patterned in hydrogen silsesquioxane (HSQ) resist using a Vistec VB6 electron beam lithography tool. After development in tetramethylammonium hydroxide (TMAH), the samples were etched in a mixed SF_6 and C_4F_8 recipe [23], through the Ge epilayer to the Si substrate, leaving ∼ 560 nm tall pillars, as measured by scanning electron microscopy (SEM), Fig. 1. Both 300 and 200 nm

#235529 Received 12 Mar 2015; revised 14 Apr 2015; accepted 3 May 2015; published 6 Jul 2015

squares were patterned with 200 nm gaps. This gives a dense pattern to maximize signal intensity, while leaving sufficient space for lateral increase in pillar width following the silicon nitride stressor layers deposition.

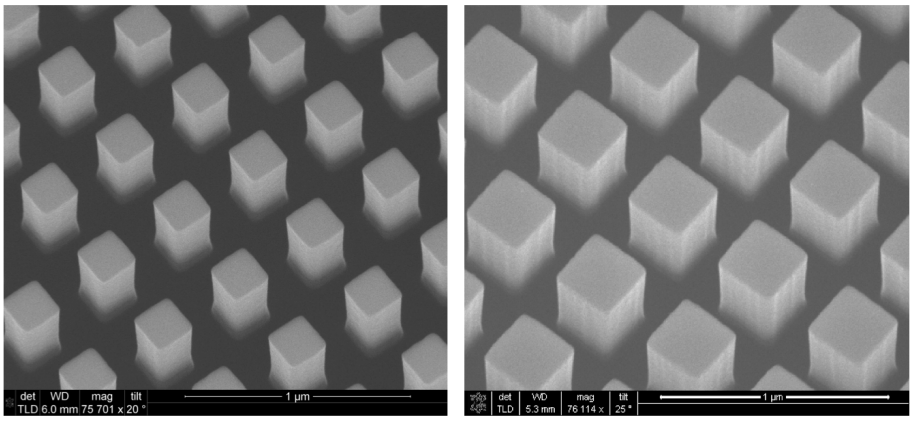

Fig. 1. Scanning electron microscope images of 200 nm square top Ge nanopillars (left) and 300 nm square top Ge nanopillars (right) after the removal of HSQ resist.

High stress silicon nitride layers were deposited using an Oxford Instruments PlasmaPro System 100 ICP tool. The radius of curvature of a 100 mm (100) Si wafer is measured, using a surface profiler, before and after the deposition of a high stress silicon nitride layer. This allows the stress of the film to be calculated using Stoney's equation (Eq. (1)), where E_s is the Young's modulus of the substrate, t_s is the substrate thickness, t_f is the film thickness, ν is Poisson's ratio for the substrate, and R_{pre} and R_{post} are the pre deposition and post deposition radii of curvature respectively. The silicon nitride film thickness was measured by selectively stripping the film, allowing for the step-height to be measured with a surface profiler. Film thickness measurements were further confirmed by ellipsometry. An increase in the stress of the film was observed with increasing platen power in the deposition tool.

$$\sigma = \frac{E_S\, t_S^2}{6(1-\nu_s)t_f}\left(\frac{1}{R_{post}} - \frac{1}{R_{pre}}\right) \tag{1}$$

Three samples containing 300 nm and 200 nm square pillar arrays were deposited with silicon nitride layers of three different levels of stress. A silicon nitride layer with negligible stress was deposited on the reference sample, while the other two samples were coated with high stress layers. The two high stress layers were measured to have compressive stresses of 1.9 GPa, and 2.7 GPa respectively. The compressive stress in the film transfers tensile strain to the underlying feature when it relaxes. All film thicknesses were $\sim$ 150 nm as measured by ellipsometery on the sample edge.

4. Optical characterisation

A Bruker Vertex 70 Fourier Transform Infrared Spectroscopy (FTIR) system was used to measure the photoluminescence of the Ge nanopillar samples, with a diode pumped continuous wave (cw) solid state laser emitting at 532 nm used to optically pump the samples. The FTIR system was operated in step-scan mode, using a 1 kHz optical chopper and a lock-in amplifier to discriminate against ambient blackbody heating. The laser illuminates the sample through an aperture in a parabolic mirror. The sample emission is then collected by this mirror, which

#235529 Received 12 Mar 2015; revised 14 Apr 2015; accepted 3 May 2015; published 6 Jul 2015

couples the emission into the internal Michelson interferometer of the FTIR system. The sample emission collected is therefore surface normal, which has implications for the interband transitions that can be measured due to selection rules; this is discussed further below. When pumping significantly above the band-edge in energy, even at low power densities, heating can be observed in the form of blackbody emission.

After the ambient blackbody is removed by the step-scan measurement, a visible tail is left, which is the differential blackbody emission caused by this heating. The pump power was varied with neutral density filters to confirm that this heating was not sufficient to redshift the emission, which is to be expected for such low pump power densities ($\sim$ 30 W cm^{-2}). In order to improve the signal to noise ratio, multiple step-scan measurements were run and subsequently averaged, for each measurement.

An advantage of using a reference sample with a silicon nitride coating is that any effects from the periodicity of the array including the presence of the silicon nitride would be visible in the unstrained sample. In order to confirm there were no such optical effects, the sample stage was tilted at various angles between 0 and $\sim 50^\circ$ away from surface normal in order to verify that there was no change to the measured spectra from diffraction. These considerations allow spectral peaks to be uniquely identified as interband transitions in the work reported below.

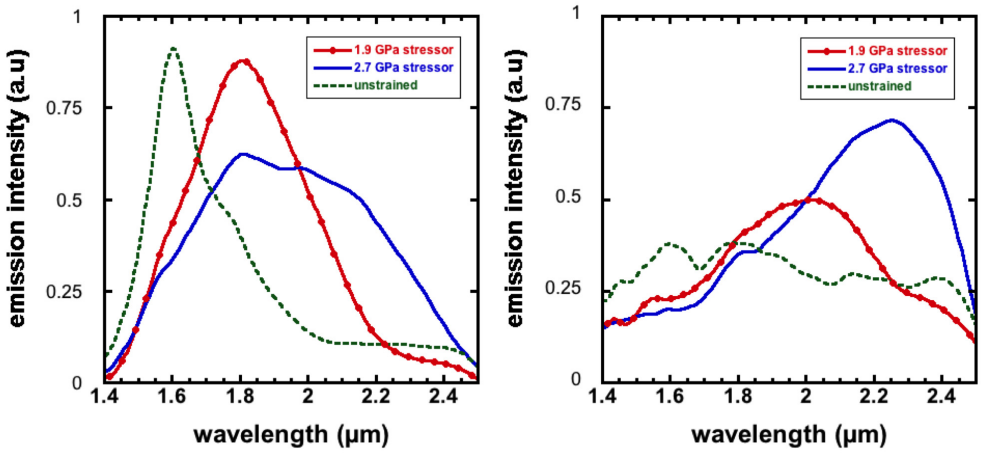

Fig. 2. The photoluminescence from 300 x 300 nm pillars (left) and 200 x 200 nm pillars (right), with variable levels of stress in the silicon nitride stressor layers.

In all strained samples, the emission wavelength was found to redshift, as expected. The 300 nm pillars with 2.7 GPa stressors, demonstrate a peak at $\sim$1.98 μm, assumed to be the Γ-valley to light-hole (LH) emission. Accounting for bandgap narrowing of 32 meV, this would suggest biaxial equivalent strain levels of approximately 0.9 % from deformation potentials [11]. Complex carrier diffusion mechanisms within a single pillar makes it difficult to estimate which area of the pillar the photoluminescence predominantly stems from. The 532 nm pump is likely to be absorbed within the first 20 nm of the surface, however as discussed by Pezzoli et al. in [24], in unstrained Ge pillars, carriers will diffuse throughout the full structure under steady state illumination, particularly with the high recombination velocities towards threading dislocations. Broad emission spectra from the 300 nm, with a small shoulder at $\sim$ 1.6 μm, suggests that there is photoluminescence from the full pillar, however with enhanced radiative recombinations from the highest strained regions. Consistent with common deformation potentials [18, 11, 25], the L-valley to heavy-hole (HH) emission appears relatively constant, at just above 1.8 μm as demonstrated in Fig. 2. Further to the peak visible at $\sim$ 1.98 μm, the broad

#235529 Received 12 Mar 2015; revised 14 Apr 2015; accepted 3 May 2015; published 6 Jul 2015

emission at longer wavelength is likely to be from L to LH transitions.

For the 200 nm pillars, the photoluminescence was found to be significantly reduced in intensity compared to the 300 nm pillars. This can be explained by the reduction in fill factor compared to the 300 nm pillars, as well as increased surface area per volume of Ge and therefore increased surface non-radiative recombination. In this instance, the photoluminescence from interband recombination from the reference sample is of a similar intensity to the differential blackbody heating, which is visible in Fig. 2. Despite a reduced emission intensity, however, a red-shift can also be observed with increased stress in the silicon nitride layers. For the highest levels of stress, emission at a peak wavelength of $\sim 2.25\,\mu$m is visible. When accounting for bandgap narrowing and assuming Γ to LH emission, this relates to a biaxial equivalent tensile strain of up to $\sim 1.35\%$. Once again, indirect transitions may contribute to emission. As expected, strain appeared to increase in smaller samples for a given stressor layer, as the stress in the film can transfer more fully into the underlying structure. Increased strain in smaller structures has indeed been reported elsewhere [17]. As discussed previously, with carrier diffusion throughout the structure, the larger total shift of the spectra, compared to the broadening seen with the 300 nm pillars could be a hallmark of more uniform strain. Strained emission from these samples is more highly red shifted than previous reports using silicon nitride stressor layers [14–17].

Particularly for the 300 nm pillars, no increase in emission intensity was observed, at variance to various other works [13, 16, 17]. This is attributed in part to the polarization of the Γ-valley to LH transition. At 0.9% biaxial strain emission from this transition is highly polarized parallel to the pillar axis (in-plane TM-component), which our experimental set-up is weakly sensitive to. The predominance of such polarization in highly strained Ge has indeed been reported by Nam et al. in [26]. Scattering processes, however, do make it conceivable that Γ to LH emission is observable with surface normal collection, compounded by the fact that stressors are expected to increase the non-parabolicity of the HH and LH bands, which is known to relax the polarization selection rules [27, 28]. The apparent decrease in intensity from the 300 nm pillars with 1.9 GPa stressors, to the 300 nm pillars with 2.7 GPa stressors, can be partly explained by considering the interband transitions that contribute to the PL. In the 1.9 GPa stressor sample, the peak at 1.8 μm is likely contributed to by direct and indirect transitions. In contrast, at higher levels of strain, the Γ to LH transition has moved to longer wavelengths, and therefore no longer contribute to emission around 1.8 μm. However, when looking at the total integrated intensity of this emission, this difference would not appear to be so significant. This is further complicated by the above arguments regarding polarization of this transition at different strain levels [26]. As discussed previously with regard to the 200 nm pillars, the more total shift of the spectra suggests more uniform strain. Thus, a larger volume of the pillar is contributing to the emission at longer wavelengths, and could account for the small intensity increase despite the polarization considerations. However, there is still difficulty in formally analyzing the intensity of the strained samples emission for these geometries, as the addition of silicon nitride stressor layer alters the amount of reflected pump power, as well as the proportion of out-coupled light from the nano-structures, and also, some of the TM polarized light may be reabsorbed by adjacent pillars before it can be scattered out to the surface normal direction. No attempt has therefore been made to quantitatively compare the relative intensities of the strained emission, which would only be practical when measuring a single pillar, and collecting emission from various polarizations.

5. Raman spectroscopy

Raman measurements were undertaken with a WITec Alpha 300 RAS confocal microscope using an excitation wavelength of 532 nm. Individual 300 nm pillar structures could clearly be

#235529 Received 12 Mar 2015; revised 14 Apr 2015; accepted 3 May 2015; published 6 Jul 2015

resolved by both the signal intensity and by the relative Raman shift, which varied from the pillar tops to the gaps between the pillars. Strain values were approximated using values of the phonon deformation potentials [29], which lead to a biaxial strain shift coefficient of b_{bi} = -424 cm^{-1}.

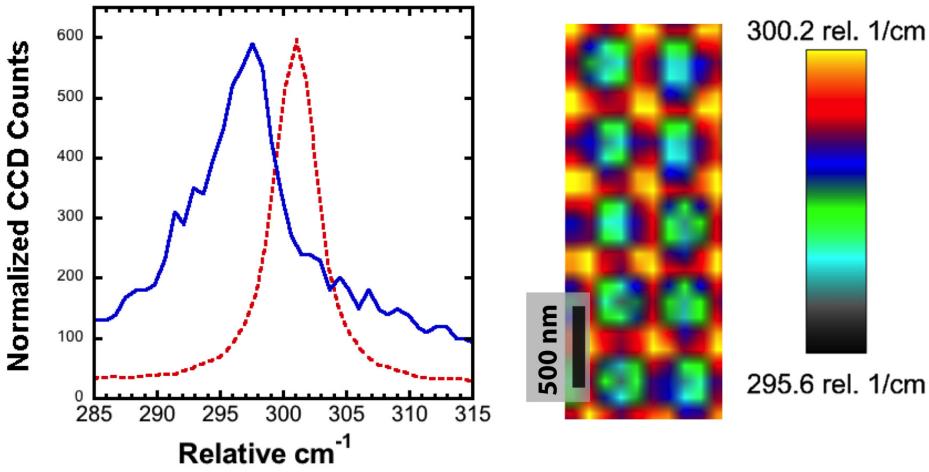

Fig. 3. Left: The Raman line of the blank unpatterned Ge following growth (red dashed line), demonstrating no visible strain. Also plotted is the Raman line for the 300 nm square top Ge nanopillar stressed with a 2.7 GPa silicon nitride stressor layer (blue solid line). The two peaks have been normalized to similar intensities to allow an easy comparison. Right: The Raman map of 300 nm pillars. Each spectrum is fitted with a Lorentzian to form the colour map.

The measurement was carried out at low powers (<2 mW before the 100 x NA 0.9 objective) and comparatively long integration times of 0.5 s per spectrum, due to the sensitivity of the pillars to laser heating from the focused spot. In the backscatter geometry with (100) Ge, only the longitudinal optical (LO) phonon should be measured and should be independent of the polarization of the source [30]. 300 nm pillars showed clear single peaks, however Raman spectra from the 200 nm pillars could not be fitted with a single Lorentzian. This is likely due to the spatial resolution of the system, and the low signal to noise ratios observed for this measurement. For the system used, the resolution was proven to be at the level of the FWHM of the airy disk ($FWHM_{Airy}$ = 0.51*λ/NA = 301 nm). Given the 200 nm pillars have 200 nm gaps there are many positions where both the top of the pillar and the sides are simultaneously recorded which could potentially explain these results. Also, due to the height of the pillars (∼560nm) compared to the depth resolution of the confocal Raman system used (FWHM ∼750nm) it is feasible to assume, that both the top of the pillars and the valleys were in focus. Due to these factors, the Raman measurements from the 200 nm pillars will no longer be discussed.

The Raman measurements on the 300 nm pillars demonstrated finite variation from pillar to pillar, which further explains the broadness of the emission in the photoluminescence. It is likely, however, that the pillars with the highest strain levels would have increased radiative efficiencies and as a result it is not surprising that clear peaks are still discernible in the photoluminescence. Raman maps were examined, and spectra were extracted from pillars demonstrating the highest strain in the measurement area. Once fitted with a single Lorentzian, a peak position at 296.3 cm^{-1} was found as demonstrated in Fig. 3. This corresponds to a biaxial tensile strain of 0.91% from phonon deformation potentials, and is therefore in excellent agreement with the

#235529 Received 12 Mar 2015; revised 14 Apr 2015; accepted 3 May 2015; published 6 Jul 2015

strain estimated from the peak position of the PL using deformation potentials [11].

While assumptions of biaxial strain for the deformation potentials and the Raman shift appeared to be extremely consistent, any deviation from purely biaxial strain has the potential to introduce significant error to the assumed level of strain, which can be seen by the dependance of the Raman line on all three components of the tensor trace, Eq. (2). Therefore, modelling of the strain distribution is required, which is discussed in the follow section.

$$\Delta\omega = \frac{1}{2\omega_0}[p\varepsilon_{zz} + q(\varepsilon_{xx} + \varepsilon_{yy})] \tag{2}$$

$$\Delta\omega = \frac{1}{\omega_0}(-p\frac{C_{12}}{C_{11}} + q)\varepsilon_{xx} \tag{3}$$

$$\Delta\omega = -b_{bi}\varepsilon_{xx} \tag{4}$$

6. Modelling

Finite element modelling software (Comsol Multiphysics) was used to simulate the strain distribution in a 300 nm Ge nanopillar. Ge pillars were modelled using an anisotropic elasticity tensor, with the [100] crystallographic direction aligned to the *x*-direction in the model. Silicon nitride layers were pre-stressed with the experimentally measured value of stress from the curvature measurements. A cross sectional transmission electron microscopy (TEM) image of 300 nm pillars was used to measure the ratio of the silicon nitride on the pillar top to the pillar sides which was found to be around $\sim$ 3:1, and was taken into account in the model. Certain parameters such as the Young's modulus of the silicon nitride have been not been measured, and therefore the model is primarily used to understand the strain distribution rather than confirm the absolute measured value. A Young's modulus of 100 GPa was used, in keeping with modelling by Ghrib et al. in [16] using high stress silicon nitride layers.

On the top surface, the pillar centres are biaxially strained with ε_{xx} = ε_{yy} = 0.68 %. This underestimates the strain when assuming a biaxial model with the assumption that:

$$\varepsilon_{zz} = -2\frac{C_{12}}{C_{11}}\varepsilon_{bi} \tag{5}$$

It was found, however, that the presence of the silicon nitride on the sidewalls counteracts the compression in the *z*-direction from Eq. (5), i.e. $\varepsilon_{zz} > -2\frac{C_{12}}{C_{11}}\varepsilon_{bi}$. As a result, the model demonstrates that an all around silicon nitride stressor in this instance increases the hydrostatic component of the strain, which from deformation potential theory, is known to move the bands at a greater rate than purely biaxial strain.

When directly using the values of ε_{xx}, ε_{yy}, and ε_{zz} from the model, and calculating the Raman line using Eq. (2), a Raman line of 296.56 cm^{-1} is calculated at the pillar top (Fig. 4) when taking into account the weighted contribution over the absorption depth of the 532 nm source, using the correction presented by Wolf et al. in [31] . This is in good agreement with the measured Raman line of 296.3 cm^{-1}. Furthermore, using these tensor components and calculating the band edges using deformation potentials, the Γ-valley to LH emission is calculated to be 1.96 μm, after correcting for 32 meV BGN from degenerate doping. This is again in excellent agreement with the emission observed at $\sim$ 1.98 μm.

As stated previously, the model was not intended to confirm the level of strain, however, the nature of the strain distribution would appear to be consistent with the experimental results. Fig. 4 demonstrates the calculated difference between a top-surface only stressor and an all around stressor layer - highlighting the impact of the sidewall stressors. This difference is demonstrated in the form of the calculated Raman line, as well as the Γ to LH transition and the

#235529 Received 12 Mar 2015; revised 14 Apr 2015; accepted 3 May 2015; published 6 Jul 2015

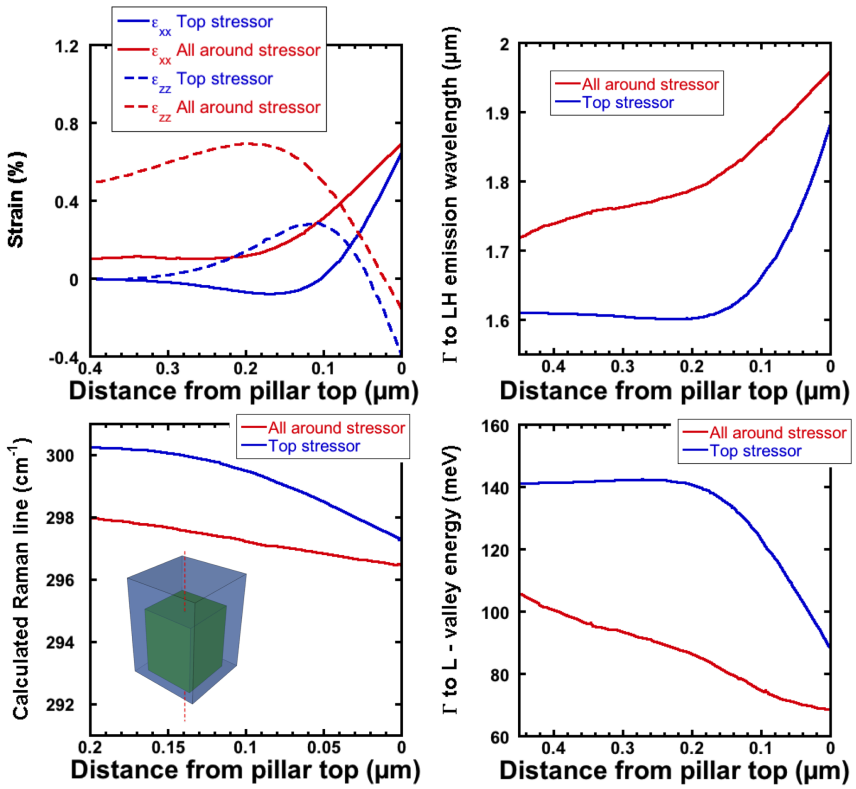

Fig. 4. Calculated comparisons between 300 nm square top Ge pillars with; an all around 2.7 GPa silicon nitride stressor layer, and a top only 2.7 GPa silicon nitride stressor layer. All calculations are from a line segment through the centre of the pillar, as shown in the illustration at the inset of the bottom left plot. Top Left: Calculated ε_{xx} (= ε_{yy}) and ε_{zz}. Top right: Calculated Γ to LH emission wavelength using deformation potentials. Bottom Right: Calculated difference between the Γ and L valleys, demonstrating that the addition of silicon nitride on the pillar sidewalls produces a significant decrease in the energy difference between the valleys, and is therefore closer to direct bandgap than with a top stressor. Bottom left: The calculated Raman line using Eq. (2), and an illustration indicating the line segment (in the z direction) down which the calculations were performed.

Γ to L energy difference. The Γ to LH transition includes the 32 meV BGN from degenerate n-type doping. It is clear from Fig. 4 that not only does the presence of the silicon nitride on the sidewalls significantly decrease the energy difference between the Γ and the L valleys, but also there is a visibly reduced gradient in the vertical direction down the pillar.

While the strain levels have been compared to their biaxial equivalents in terms of Γ to LH emission, it is worth noting that an increased hydrostatic component of the strain causes a difference in the band structure when compared to purely biaxial. For instance, comparing the modelled strain at the top plane of a 300 nm pillar with ε_{xx} = ε_{yy} = 0.68 %, and ε_{zz} = -0.15 %, to a biaxial strain of 0.9 %, both have Γ to LH bandgaps of 667 meV. However, in the pillar geometry the Γ to L difference is 69 meV compared to 79.8 meV with biaxial strain, i.e. the pillar is closer to direct bandgap. This is significantly advantageous because the required doping to move the Fermi level to the Γ is reduced compared to biaxial strain. A further difference is due to the fact the increased hydrostatic component maintains more of the unstrained crystal

#235529 Received 12 Mar 2015; revised 14 Apr 2015; accepted 3 May 2015; published 6 Jul 2015

symmetries. This effect results in a lower valence band splitting than with biaxial strain, with LH to HH energies of 38 meV in the 300 nm pillar compared to 67.9 meV with biaxial strain.

7. Conclusions

High strain levels of up to $\sim$ 1.35 % biaxial equivalent have been demonstrated in Ge on Si nanopillars with silicon nitride stressor layers, demonstrating that in certain geometries this technique can be used to red-shift the Ge band-edge by up to 0.65 μm from the degenerately doped band-edge at 1.6 μm. Photoluminescence from 300 nm nanopillars containing 0.9 % biaxial equivalent tensile strain demonstrate clear discernible peaks which have been attributed to direct and indirect interband transitions. The level of strain measured from the PL has been confirmed by confocal Raman microscopy, and finite element modelling provides an insight into the strain distributions in the pillar. The presence of silicon nitride on the pillar sidewalls appears to increase the hydrostatic component of the strain with respect to a top only stressor layer. As such, despite calculated strains of ε_{xx} = ε_{yy} = 0.68 % at the top plane, the increase in ε_{zz} leads to a band-edge comparable to 0.9 % biaxial strain in terms of Γ to LH emission. Furthermore, the increased hydrostatic strain demonstrated in the model would suggest a Γ to L energy difference comparable to 0.97 % biaxial strain, which highlights the potential advantage of this type of strain distribution. Furthermore, models of the all around stressors demonstrate a reduced strain gradient compared to a top only stressor, which is potentially key to high performance Ge lasers, when trying to maximize the optical overlap with the gain region.

Acknowledgments

The authors would like to thank the staff of the James Watt Nanofabrication Centre for help with the fabrication. The work was funded by U.K. EPSRC (Project no. EP/H02364X/1) and EC GEMINI (Project No. 613055).

#235529 Received 12 Mar 2015; revised 14 Apr 2015; accepted 3 May 2015; published 6 Jul 2015